Pergamon

Calphad Vol. 20, No. 4, pp. 447–460, 1996

0364-5916/96 $15.00 + 0.00

PII S0364-5916(97) 00007-2

KINETICS OF PRECIPITATION IN POWER PLANT STEELS

J. D. Robson and H. K. D. H. Bhadeshia
University of Cambridge

(Presented at CALPHAD XXV, Erice, Sicily, Italy, May 1996)

ABSTRACT

The ability of steels to resist creep deformation depends on the presence in the microstructure of carbide and intermetallic compounds which precipitate during tempering or during elevated temperature service. The precipitation occurs in a sequence which leads towards thermodynamic equilibrium. Kinetic theory has recently been developed which enables such sequences to be modelled using an adaptation of the classical Johnson–Mehl–Avrami equations. Our modification permits the treatment of more than one precipitation reaction occurring simultaneously, a feature which is essential for the reactions observed experimentally in a wide range of secondary hardening steels. In this paper, the model is applied to a series of power plant steels. It is possible to explain some interesting differences between the steels as a function of the chemical composition.

Introduction

Steels used in the manufacture of power plant range from those designed to resist creep deformation at temperatures around 600 °C, to others which are exposed to relatively low temperatures where the primary design criterion is toughness (1,2). The microstructures of power plant alloys often consist of δ–ferrite, martensite, bainite, allotriomorphic ferrite and retained austenite as the major phases obtained following a normalising heat–treatment. However, these microstructures are then subjected to very severe tempering ($\simeq$ 700 °C, several hours) causing general coarsening and the precipitation of ever more stable alloy carbides and intermetallic compounds. It is these solid–state reactions which ultimately determine the mechanical stability of the steels, and hence their useful design lives.

Calculations of the phase diagram for multicomponent steels have helped greatly in the design of power plant steels (3,4). However, these calculations refer to the equilibrium state, and even though they can be adapted to deal with constrained equilibria, they are not on their own sufficient to model the sequence of precipitation reactions. After all, the set of reactions which leads towards equilibrium occurs in the first place because kinetic difficulties prevent the direct formation of the equilibrium microstructure. A further complication is that the formation of metastable precipitates alters the chemical composition and hence the thermodynamic driving force for any subsequent reactions. Consequently, any kinetic theory must be able to deal with the simultaneous precipitation of several interacting phases rather than just *successive* reactions.

Progress has recently been made on a kinetic theory for simultaneous reactions (5,6). The classical

Original version received on 20 June 1996, Revised version on 11 November 1996

Johnson–Mehl–Avrami theory describing the rate at which a phase precipitates during solid–state transformation has been adapted to deal with the simultaneous precipitation of many phases. In the simplest of cases, where the fractions of the product phases are related by constants, it has been possible to solve the problem rigorously. An approximate method has been necessary to deal with cases where the composition of the matrix changes during the course of the transformations. The method in principle enables any number of simultaneous precipitation reactions to be modelled theoretically, relying only on the availability of interfacial energies, number densities of nucleation sites and thermodynamic data. It is possible therefore to attempt a prediction of the time–temperature–transformation diagram for tempering reactions in secondary–hardening steels as a function of the chemical composition and heat treatment.

The purpose of the present work was to use the new method in order to understand the role of alloying elements in the design of modern power plant steels. The theory has therefore been used to predict the precipitation kinetics for four types of power plant steel, a $2\frac{1}{4}$Cr1Mo steel, a 3Cr1.5Mo steel, a 9CrMoWV steel and a 10CrMoV steel.

Kinetics of Simultaneous Reactions

The evolution of volume fraction during solid–state transformation can be modelled using the classical Johnson–Mehl–Avrami theory, which has been reviewed by Christian (7). This approach is limited to the formation of a single phase and can only be applied to problems involving more than one phase if the individual reactions occur successively and largely independently (8-10). A great deal of fruitless work demonstrated that the evolution of carbides during the tempering of steels cannot be treated in this way. Precipitation and dissolution reactions during tempering overlap significantly, with profound interactions between the different precipitates. Consequently, we have adapted the Johnson–Mehl–Avrami approach to deal with many reactions occurring simultaneously. The principals involved are first illustrated with a simplified example in which β and θ precipitate at the same time from the parent phase which is designated α. It is assumed that the nucleation and growth rates do not change with time and that the particles grow isotropically.

The increase in the extended volume due to particles nucleated in a time interval $t = \tau$ to $t = \tau + d\tau$ is, therefore, given by

$$dV_\beta^e = \frac{4}{3}\pi G_\beta^3 (t-\tau)^3 I_\beta(V)\, d\tau \tag{1}$$

$$dV_\theta^e = \frac{4}{3}\pi G_\theta^3 (t-\tau)^3 I_\theta(V)\, d\tau \tag{2}$$

where G_β, G_θ, I_β and I_θ are the growth and nucleation rates of β and θ respectively, all of which are assumed here to be independent of time. V is the total volume of the system. For each phase, the increase in extended volume will consist of three separate parts. Thus, for β:

(i) β which has formed in untransformed α.

(ii) β which has formed in regions which are already β.

(iii) β which has formed in regions which are already θ.

Only β formed in untransformed α will contribute to the real volume of β. On average a fraction $\left(1 - \frac{V_\beta + V_\theta}{V}\right)$ of the extended volume will be in previously untransformed material. It follows that the

increase in real volume of β is given by

$$dV_\beta = \left(1 - \frac{V_\beta + V_\theta}{V}\right) dV_\beta^e \tag{3}$$

and similarly for θ,

$$dV_\theta = \left(1 - \frac{V_\beta + V_\theta}{V}\right) dV_\theta^e \tag{4}$$

Generally V_β will be some complicated function of V_θ and it is not possible to integrate these expressions to find the relationship between the real and extended volumes. However, in certain simple cases it is possible to relate V_β to V_θ by multiplication with a suitable constant, K. It is then possible to write

$$V_\theta = KV_\beta \tag{5}$$

The equations relating the increment in the real volume to that of the extended volume may now be written as

$$dV_\beta = \left(1 - \frac{V_\beta + KV_\beta}{V}\right) dV_\beta^e \tag{6}$$

$$dV_\theta = \left(1 - \frac{V_\theta + KV_\theta}{KV}\right) dV_\theta^e \tag{7}$$

Equations 6 and 7 may then be integrated to find an analytical solution relating the extended and real volumes analogous to that for single phase precipitation.

$$\frac{V_\beta^e}{V} = \frac{-1}{1+K} \ln\left(1 - \frac{V_\beta}{V}(1+K)\right) \tag{8}$$

$$\frac{V_\theta^e}{V} = \frac{-K}{1+K} \ln\left(1 - \frac{V_\theta}{V}\left(\frac{1+K}{K}\right)\right) \tag{9}$$

The total extended volume is found for each phase by integrating equations 8 and 9 with respect to τ. After rearranging, the final expressions for the volume fractions of β and θ phases (ζ_β and ζ_θ) are

$$\zeta_\beta = \left(\frac{1}{1+K}\right)\left(1 - \exp\left(-\frac{1}{3}(1+K)\pi G_\beta^3 I_\beta t^4\right)\right) \tag{10}$$

$$\zeta_\theta = \left(\frac{K}{1+K}\right)\left(1 - \exp\left(-\frac{1}{3}\left(\frac{1+K}{K}\right)\pi G_\theta^3 I_\theta t^4\right)\right) \tag{11}$$

These equations resemble the well known Avrami equation for single phase precipitation with extra factors to account for the presence of a second precipitate phase. When the volume fraction of both precipitating phases is very small equations 10 and 11 approximate to the expressions for each phase precipitating alone. This is because in the early stages of transformation nearly all of the extended volume lies in previously untransformed material and contributes to the real volume. As transformation proceeds, the volume fraction of each phase predicted for the phases precipitating simultaneously becomes less than that predicted if the phases were precipitating alone. This is what is expected, since additional phases reduce the fraction of the extended volume which lies in previously untransformed material.

Since the nucleation and growth rates were assumed to be constant, it is possible to calculate explicitly the value of K. The volume of each phase at any time depends on its nucleation rate and the cube of its growth rate. The ratio V_θ/V_β is then constant and given by

$$K = \frac{V_\theta}{V_\beta} = \frac{I_\theta G_\theta^3}{I_\beta G_\beta^3} \tag{12}$$

Some example calculations for the case of linear (*i.e.* constant) growth are presented in Fig. 1. When the nucleation and growth rates of β and θ are set to be exactly identical, their curves for volume fraction versus time are exactly superimposed and each phase eventually achieves a fraction of 0.5 (Fig. 1 a). When the nucleation rate of β is set to equal twice that of θ, then for identical growth rates, the terminal fraction of β is, as expected, twice that of θ (Fig. 1 b). The case where the growth rate of β is set to be twice that of θ (with identical nucleation rates) is illustrated in Fig. 1 c. The final volume fraction of the β phase is eight times that of the θ phase because volume fraction is a function of the growth rate cubed.

Complex Simultaneous Reactions

In practice, the multiple reactions found in power plant steels have important complications not included in the simple model described above. The phases interfere with each other not only by reducing the volume available for transformation, but also by removing solute from the matrix and changing thereby changing its composition. This change in matrix composition changes the growth and nucleation rates of the phases. There are no simple constants linking the volume fractions of all the phases and a different approach is needed. A model has therefore been developed to treat the kinetics of simultaneous transformations in power plant steels based on the principles outlined above but with several additional features. The main features of the model are summarised below, a full description is given in reference (5).

- The model allows for the simultaneous precipitation of M_2X, $M_{23}C_6$ and Laves phase. M_3C is assumed to nucleate instantaneously with the paraequilibrium composition (11). Subsequent enrichment of M_3C as it approaches its equilibrium composition is accounted for.
- All the phases, except M_3C, form close to their equilibrium composition. The driving forces and compositions of the precipitating phases are calculated using MTDATA (12).
- The interaction between the precipitating phases is accounted for by considering the change in the average solute level in the matrix as each phase forms.
- The model does not require prior knowledge of the precipitation sequence.

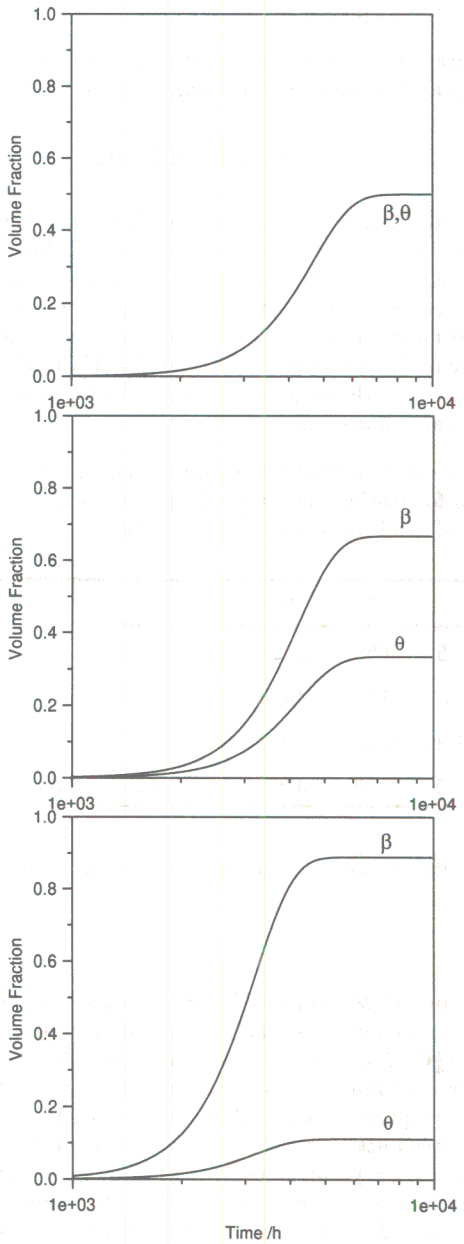

Fig. 1 : Simultaneous precipitation of θ and the β (a) When the two phase have identical nucleation and growth rates. (b) Identical growth rates but with the β having twice the nucleation rate of θ. (c) Identical nucleation rates but with β particles growing at twice the rate of the θ particles.

- Dissolution of non–equilibrium phases is incorporated.
- A single set of fitting parameters for the nucleation equations (site densities and surface energies) has been found which is applicable to a wide range of power plant steels.

Results and Discussion

The simultaneous kinetics model has been applied to four different power plant steels which span a wide composition range. The compositions of these steels are shown in Table 1. The first alloy, $2\frac{1}{4}$Cr1Mo steel is an incredibly popular steel used throughout the world, for power plant where the steam temperature does not exceed about 565 °C. It has a microstructure which after normalising is a mixture of carbide–free bainite, retained austenite and martensite. The 3Cr1.5Mo alloy has a similar microstructure but is more modern and is designed to give a higher strength variant of the $2\frac{1}{4}$Cr1Mo steel (13,14,15). The remaining two steels are both martensitic but with much larger chromium concentrations and are designed for even higher temperature creep–critical applications.

The combination of these steels covers virtually the entire range of common power plant steels; they form therefore, a good set of alloys for testing and calibrating the model. It was also hoped that the model might reveal more clearly the effect of individual alloying additions on the nature of carbide precipitation.

	C	Mn	Cr	Mo	Ni	V	Nb	W	Fe
$2\frac{1}{4}$Cr1Mo	0.15	0.50	2.12	0.9	0.17	–	–	–	bal
3Cr1.5Mo	0.1	1.0	3.0	1.5	0.1	0.1	–	–	bal
9CrMoWV	0.106	0.45	8.96	0.47	–	0.20	0.069	1.83	bal
10CrMoV	0.11	0.50	10.22	1.42	0.55	0.20	0.50	–	bal

Table 1 : Concentration (in weight%) of the major alloying elements in the steels used to demonstrate the model

Transmission electron microscopy (TEM) studies of heat treated samples of the 10CrMoV alloy, described elsewhere (6), were used to build up a carbide stability diagram for this steel, analogous to that produced by Baker and Nutting for the $2\frac{1}{4}$Cr1Mo steel (16). As well as recording whether or not a particular phase was observed, volume fractions were also measured and used to provide data with which to calibrate the model. The measured points are plotted in Fig. 2 along with TTT lines predicted by the model. The lines for $M_{23}C_6$ and M_2X have been fitted to the measured volume fractions at 600 °C. The line for Laves phase was predicted using the fitting parameters derived from experimental data from the 9CrMoWV alloy (see Fig. 5). The fitting parameters are shown in Table 2. It may yet be possible that a different set of parameters could adequately describe the experimental data. However, it is noteworthy that the interfacial energy correlates with the known position of the phase concerned in the precipitation sequence. It is important to note that the same set of parameters has been used to make predictions for all the steels, even though the precipitation kinetics are known to be vastly different.

Phase	Surface Energy/J m^{-2}	Site Density/m^{-3}
M_2X	0.248	2.7×10^{16}
$M_{23}C_6$	0.269	2.7×10^{15}
Laves	0.331	2.7×10^{8}

Table 2: Values for surface energy and site density for nuclei of each phase which give the best fit between prediction and experiment

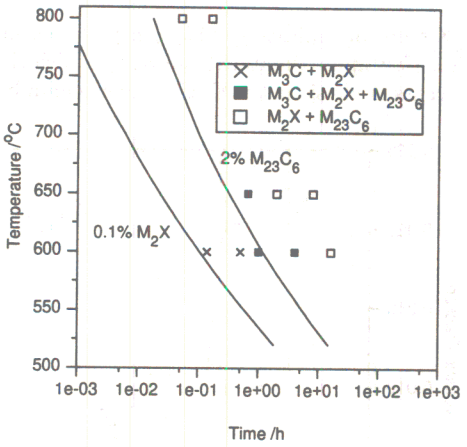

Fig. 2 : Predicted TTT diagram for a 10CrMoV steel. Superimposed are points corresponding to experimental observations.

The equilibrium phases, as calculated using MTDATA, for all the steels under investigation are shown in Table 3. Fig. 2 shows that the model predicts that Laves phase will only form in the 10CrMoV steel below approximately 550 °C. MTDATA predicts that the maximum temperature that Laves phase could reach an equilibrium volume fraction of 0.0025 by thermodynamic constraints alone is 560 °C. The predicted line is consistent with this calculation and the results seem reasonable although at present there are no suitable experimental data for comparison.

The time–temperature–transformation (TTT) diagram shown in Fig. 2 was generated by producing volume fraction vs. time data for a range of temperatures and finding the time at which the volume fraction reached a certain value (*e.g.* 0.02 for $M_{23}C_6$). It is also possible to plot the volume fraction of each phase as a function of time at any temperature to give more detailed information regarding the evolution of each phase. Such a plot for the 10CrMoV steel at 600 °C is shown in Fig. 3. The sequence of events shown may be summarised as follows; first there is rapid precipitation of M_2X which reaches its equilibrium volume fraction after approximately 15 minutes. This is accompanied by dissolution of M_3C, although

T / °C	$2\frac{1}{4}$1Mo	10CrMoV	9CrMoWV	3Cr1.5Mo
500	$M_{23}C_6$	$M_{23}C_6$,M_2X, Laves	$M_{23}C_6$,M_2X, Laves	$M_{23}C_6$,M_6C
550	$M_{23}C_6$	$M_{23}C_6$,M_2X, Laves	$M_{23}C_6$,M_2X, Laves	$M_{23}C_6$,M_6C
600	$M_{23}C_6$	$M_{23}C_6$,M_2X	$M_{23}C_6$,M_2X, Laves	$M_{23}C_6$,M_6C
650	$M_{23}C_6$	$M_{23}C_6$,M_2X	$M_{23}C_6$,M_2X, Laves	$M_{23}C_6$,M_6C
700	$M_{23}C_6$	$M_{23}C_6$, M_2X	$M_{23}C_6$,M_2X	$M_{23}C_6$

Table 3 : Predicted equilibrium precipitate phases for the steels under investigation

some M_3C remains when M_2X stops precipitating. $M_{23}C_6$ rapidly becomes the dominant carbide, reaching its equilibrium volume fraction after approximately 5 hours, by which time the M_3C has almost completely dissolved. This sequence of events is consistent with the experimentally observations, as shown in Fig. 2.

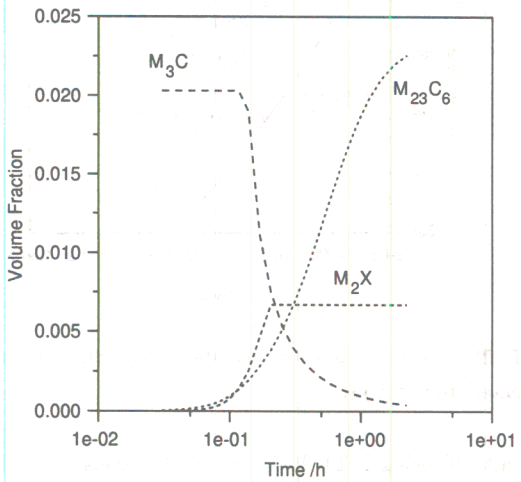

Fig. 3 : Predicted evolution of volume fraction for each phase in a 10CrMoV steel at 600 °C

A predicted TTT–diagram was then generated for the $2\frac{1}{4}$Cr1Mo alloy, using the same values for all the fitting parameters. This diagram is shown in Fig. 4. Also plotted on this diagram are the lines drawn by Baker and Nutting corresponding to the times when they first observed a phase. They do not state the volume fraction of the phase at this point, but it seems reasonable to plot lines for a volume fraction of 1% for comparison. Although the agreement between the predicted and measured results is not excellent, the model has reproduced the principal difference between the $2\frac{1}{4}$Cr1Mo and the 10CrMoV steel, which is that precipitation of $M_{23}C_6$ takes much longer in the $2\frac{1}{4}$Cr1Mo steel. It must be noted that at present the model does not allow for M_7C_3 precipitation which is observed prior to $M_{23}C_6$ formation. Allowing

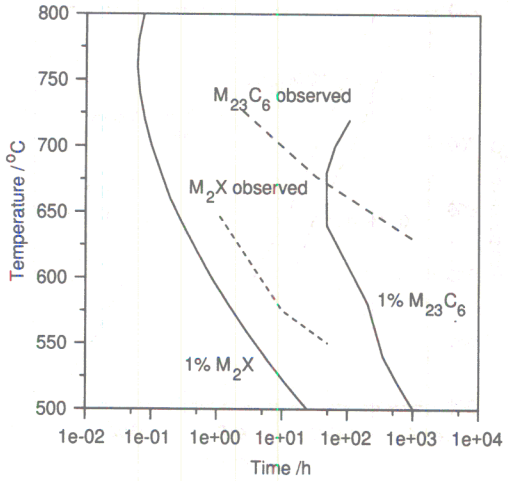

Fig. 4 : Predicted TTT diagram for a $2\frac{1}{4}$Cr1Mo steel. Also plotted are lines corresponding to when the phase was first observed by Baker and Nutting (16)

for this phase is expected to suppress $M_{23}C_6$ precipitation due to increased competition for the available solute.

Laves phase precipitation is believed to be detrimental to mechanical properties, in particular, toughness (17). To be able to model the kinetics of precipitation of this phase would be extremely useful, since it would then be possible to predict what volume fraction of Laves phase forms throughout the component lifetime. The 9CrMoWV steel (*NF-616*, composition shown in table 1) is susceptible to Laves phase formation over a relatively wide temperature range. A number of studies of Laves phase precipitation in this steel provide suitable experimental data with which to test the model (18,19). Hald (19) has developed a model for the precipitation of the Laves phase in this steel; the model begins with an assumed number density of particles which then grow at a diffusion–controlled rate. After fitting at a particular temperature, the model was applied successfully to predict the fraction of Laves phase as a function of temperature and time, taking into account changes in the equilibrium compositions and diffusivity with temperature. Fig. 5 shows a comparison of the TTT–curve for Laves phase precipitation predicted using the simultaneous kinetics model, and that predicted by Hald. The values for the surface energy and site density for Laves phase nucleation, shown in table 2, were fixed to give the best agreement between these curves. The lines for M_2X and $M_{23}C_6$ precipitation which are predicted by the simultaneous kinetics model are also plotted. It is apparent from Fig. 5 that the precipitation kinetics of M_2X and $M_{23}C_6$ are predicted to be more rapid in the 9CrMoWV steel than the 10CrMoV steel. This is at least partly due to the increased chemical driving force for precipitation of these phases in the 9CrMoWV steel, predicted using MTDATA.

Calculations were also performed for a 3Cr1.5Mo steel. The resulting TTT diagram is shown in Fig. 6 together with comparative plots of carbide fraction versus time (on the same scale) for the 3Cr1.5Mo and $2\frac{1}{4}$CrMo steels. It is evident that the speed with which $M_{23}C_6$ precipitates in the 3Cr1.5Mo alloy is very

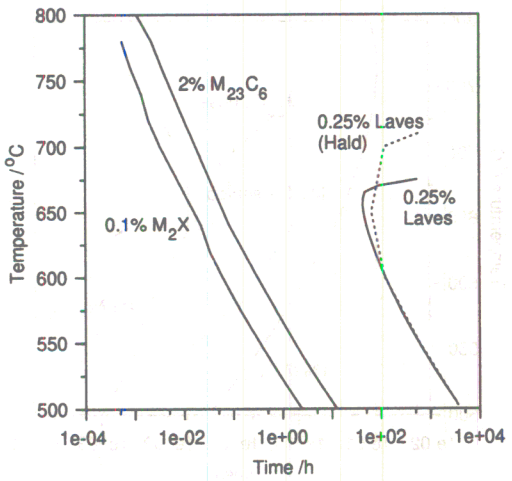

Fig. 5 : Predicted TTT diagram a 9CrMoWV steel. Also plotted is the TTT line for Laves phase precipitation predicted by Hald's model (19).

much faster than in the $2\frac{1}{4}$Cr1Mo steel and the maximum volume fraction attained by M_2C is considerably less.

These results are consistent with results reported by Klueh and Nasreldin (14). They showed that $M_{23}C_6$ formation is virtually completed within 8 hours at 688 °C in the 3Cr1.5Mo steel, whereas Baker and Nutting did not observe any $M_{23}C_6$ until after approximately 20 hours at the same temperature for a $2\frac{1}{4}$Cr1Mo steel. The plots of volume fraction evolution show that in the $2\frac{1}{4}$Cr1Mo steel the M_2C starts to precipitate well before the $M_{23}C_6$. A relatively large volume fraction of M_2C then forms which further suppresses $M_{23}C_6$ precipitation. In the case of the 3Cr1.5Mo alloy M_2C and $M_{23}C_6$ start to precipitate at similar times. Both phases are competing for solute, but the $M_{23}C_6$ dominates and M_2C starts to dissolve before it has reached a volume fraction which is sufficient to significantly delay $M_{23}C_6$ precipitation.

It is interesting to note that whilst the 3Cr1.5Mo steel has a higher Mo content that the $2\frac{1}{4}$Cr1Mo steel, the maximum volume fraction of M_2C calculated using MTDATA is significantly less (see Table 4). This is because the 3Cr1.5Mo alloy has a lower carbon content, and it is the amount of available carbon rather than molybdenum which limits M_2C formation. It was thought that it may be possible to enhance the precipitation of M_2C in the 3Cr1.5Mo steel by increasing its carbon content. This, in turn, would be expected to suppress $M_{23}C_6$ formation to longer times. To test this hypothesis calculations were performed for an alloy identical to the 3Cr1.5Mo steel, but with a carbon level of 0.15wt% (the same as in the $2\frac{1}{4}$Cr1Mo steel). Fig. 7 shows a comparison of the evolution of phases in the standard 3Cr1.5Mo0.15C steel and the carbon enriched 3Cr1.5Mo0.15C steel.

It is apparent from Fig. 7 and Table 4 that whilst the maximum possible volume fraction of M_2C is greater in the carbon enriched 3Cr1.5Mo steel the maximum volume fraction which actually forms before dissolution begins is still relatively small and is insufficient to delay $M_{23}C_6$ formation. In fact, the addition of carbon accelerates all the carbide precipitation reactions, due to an increase in the driving force for

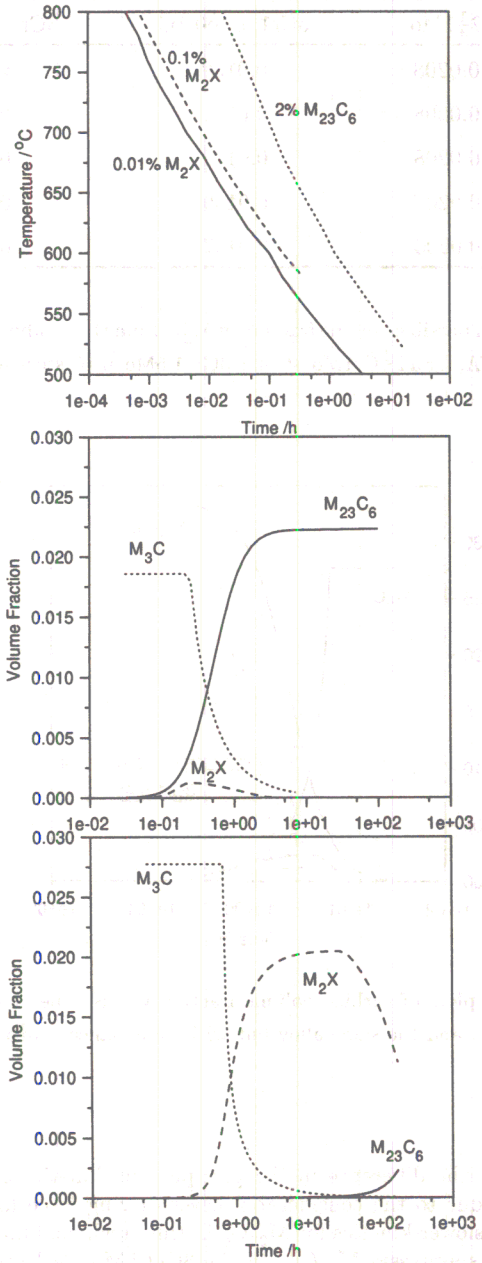

Fig. 6 : (a) Predicted TTT diagram a 3Cr1.5Mo steel. (b) Plot of carbide volume fraction versus time at 600 $°C$ for the 3Cr1.5Mo alloy. (c) Plot of carbide volume fraction versus time at 600 $°C$ for the $2\frac{1}{4}$CrMo steel.

T / °C	$2\frac{1}{4}$1Mo	3Cr1.5Mo0.1C	3Cr1.5Mo0.15C
500	0.0208	0.0139	0.0209
550	0.0208	0.0139	0.0209
600	0.0208	0.0139	0.0209
650	0.0207	0.0139	0.0208
700	0.0203	0.0137	0.0207

Table 3 : The maximum possible volume fraction of M_2C from thermodynamic constraints, predicted using MTDATA, for a $2\frac{1}{4}$Cr1Mo steel, a 3Cr–1.5Mo–0.1C steel and a 3Cr–1.5Mo–0.15C steel

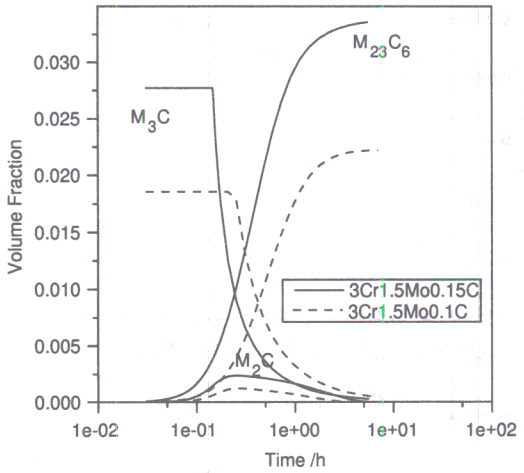

Fig. 7 : Superimposed plots of carbide volume fraction versus time at 600 $°C$, for the 3Cr1.5Mo steel (Table 1) and the same alloy but with an enhanced carbon concentration (+0.05wt% C).

carbide formation. It seems that the difference in the precipitation kinetics of $M_{23}C_6$ in the 3Cr1.5Mo steel and the $2\frac{1}{4}$Cr1Mo steel is due to the considerably lower driving force for $M_{23}C_6$ in the $2\frac{1}{4}$Cr1Mo steel (see Table 5). This leads to slower kinetics for $M_{23}C_6$ in this steel, enabling the formation significant quantities of M_2C which further suppresses $M_{23}C_6$. In the 3Cr1.5Mo steel the more rapid formation of $M_{23}C_6$ suppresses the formation of M_2C which only precipitates in small quantities before dissolution and does not significantly retard $M_{23}C_6$.

T /°C	$\Delta G/Jmol^{-1}$, $2\frac{1}{4}Cr$	$\Delta G/Jmol^{-1}$, 3Cr–0.1C	$\Delta G/Jmol^{-1}$, 3Cr–0.15C
550	-290	-394	-569
600	-248	-379	-548
650	-207	-364	-529
700	-166	-351	-509

Table 5 : A comparison of the chemical driving forces for $M_{23}C_6$ precipitation in a $2\frac{1}{4}$Cr1Mo steel, a 3Cr–1.5Mo–0.1C steel and a 3Cr–1.5Mo–0.15C steel

Conclusions

A recently developed theory for the overall transformation kinetics of simultaneous reactions has been applied, in conjunction with phase diagram calculations, towards the study the effect of alloying elements on the precipitation reactions that occur in a wide range of bainitic and martensitic power plant steels. The theory clearly reproduces experimental data with a single set of fitting parameters consisting of interfacial energies and number density of nucleation sites. For example, it is possible to predict that the formation of $M_{23}C_6$ should be orders of magnitude slower in $2\frac{1}{4}$Cr1Mo steel when compared with the 3Cr1.5Mo or 10Cr1MoV type steel. The model has also been successfully applied to a commercial 9CrMoWV alloy *NF616* where published data on Laves phase precipitation kinetics have been faithfully reproduced, taking into account the reactions which precede Laves phase formation. In the future it is intended to incorporate all the other phases into the model, particularly MX which is believed to play an important role in 9–12 wt% Cr steels.

Acknowledgements

The authors are grateful to National Power plc. for financial support via Dr. David Gooch. We would also like to thank David Gooch, Andrew Strang, Rod Vanstone and Rachel Thomson for their help during the course of some of this work. The help of Hugh Davies and Susan Hodgson with the provision and support of MTDATA is greatly appreciated. HKDHB is grateful to the Royal Society for a Leverhulme Trust Senior Research Fellowship.

References

1. K. J. Irvine: *Materials in Power Plant,* Institution of Metallurgists, London, (1975) 1–10.

2. I. M. Austin, P. McIntyre and E. F. Walker: *Materials in Power Plant,* Institution of Metallurgists, London, (1975) 120–127.

3. J. D. Robson and H. K. D. H. Bhadeshia: *Modelling the Microstructure and Properties of Advanced Power Plant Steels,* Cambridge (1995)

4. J. Hald: *Materials Comparisons Between NF616, HCM12A and TB12M, III: Microstructural Stability and Ageing,* EPRI Report (1994)